Topographically Guided UAV for Identifying Tension Cracks Using Image-Based Analytics in Open-Pit Mines

Garrett Winkelmaier, *Member, IEEE*, Rushikesh Battulwar, Mina Khoshdeli, Jorge Valencia, *Member, IEEE*, Javad Sattarvand, and Bahram Parvin, *Senior Member, IEEE*

***Abstract*—Aerial imaging of an open-pit mine integrated with the visual analytics offers a novel approach for routine monitoring of tension cracks for mine safety. Tension cracks may occur on work- or catch-benches that are excavated according to a computer aided design (CAD) model. The size of the tension cracks, their locations, and evolutions is commonly used to predict slope failures and to assure the mine safety operations. The goal of this research was to replace the current manual interventions with an automated platform for routine report generations for the mine controller. First, a drone was flown on a preprogrammed flight trajectory at a constant elevation to generate a mosaic and a depth map image. Next, work-, catch-benches, and access roads were automatically identified and represented by their medial axes. Subsequently, the waypoints from each medial axis were sequentially uploaded into the drone for scanning the corresponding regions at high-resolution. These high-resolution images were then used to delineate tension cracks. The delineation of tension cracks was performed using steerable filters, ENet, and UNet deep learning models for comparison. The ENet model, with the leave-one-out cross-validation method, produced the best performance profile with an Aggregated Jaccard Index and F1-Score of 0.51 and 0.79, respectively.**

***Index Terms*—Deep learning, image segmentation, intelligent systems.**

I. Introduction

OPEN-PIT mining is the most common mining technique for exploitation of the ore-bodies from the earth's surface. In contrast with underground mining, it provides approximately 90% of the raw mineral supplied globally. Although large and small slope failures are an inherent nature of surface mining, effective studies and monitoring of mining slopes can provide a cost effective mining operation and safe working environment. A sophisticated slope management plan reduces the slope failure risks and assures the safety of both personnel and equipment. Therefore, a comprehensive understanding of the failure phenomenon is essential and proper early warning of impending failure events must be provided by implementation of slope monitoring programs and early warning systems.

A variety of instruments could be employed for monitoring ground movements [1]. These methods for monitoring ground movements, in open-pit slopes, not only create an early warning system about upcoming failures, but also provide valuable information about their behavior. These systems can be divided into surface and subsurface categories, with a further subdivision into qualitative and quantitative systems. Every method has its own optimal niche for monitoring failure type and size [2]. Qualitative systems consist of visual inspections, which can be routine manual-inspections to detect the triggering of instability (e.g., tension cracks, excessive rockfalls) or be part of the safety checks during difficult mining situations (e.g., spotting for rockfalls). Quantitative systems usually involve instruments measuring surface or subsurface displacements. Components of surface displacement measurements can be listed in order of increasing complexity as follows [2]: cross-crack measurements and visual inspections; survey monitoring; GPS [3]; photogrammetry; laser scanning; radar, both ground-based and satellite-based (InSAR) [3], [4]; and tiltmeters and electrolevels. With respect to subsurface categories, sensors are typically installed inside the drill-holes [2] and examples are: inclinometers; short strips and time domain reflectometer (TDR) cables [5]; extensometers; thermistors; microseismic [6]; and piezometers. In addition, a slope monitoring system for a large open-pit mine may include a hybrid of the above components.

More recently, ground-based radar has become one of the leading-edge technologies for active slope monitoring due to its ability to detect movements with high accuracy, spatial coverage, and frequency of acquisition. Several successful applications of ground-based radar systems have been used to identify large-scale failures in open-pit mines [3], [4], [7]–[16]. Displacements are calculated by measuring the phase differences of the back-scattered microwave signal between two or more coherent

Manuscript received August 30, 2019; revised January 17, 2020 and March 26, 2020; accepted April 14, 2020. Date of publication May 7, 2020; date of current version February 17, 2021. This work was supported in part by the National Institute of Occupational Health and Safety (NIOSH) under Grant 200-2017-95360. *(Corresponding author: Bahram Parvin.)*

Garrett Winkelmaier, Mina Khoshdeli, and Bahram Parvin are with the Electrical and Biomedical Department, University of Nevada-Reno, Reno, NV 89557 USA (e-mail: gwinkelmaier@nevada.unr.edu; mkhoshdeli@nevada.unr.edu; bparvin@unr.edu).

Rushikesh Battulwar, Jorge Valencia, and Javad Sattarvand are with the Mackay School of Earth Sciences and Engineering, University of Nevada-Reno, Reno, NV 89557 USA (e-mail: battulwar@nevada.unr.edu; jvalencia@nevada.unr.edu; jsattarvand@unr.edu).

Color versions of one or more of the figures in this article are available online at https://ieeexplore.ieee.org.

Digital Object Identifier 10.1109/TIE.2020.2992011

acquisitions [17]–[22]. This technology presents the advantages of high measurement accuracy, high spatial and temporal resolution, long-range capabilities, and limited impact of atmospheric noise [4]. These measurements are obtained without the need to install artificial reflectors on the slopes. A comprehensive slope management system and stability analysis should include the detection and monitoring of the tension cracks on the ground surface; however, these cracks are usually not visible in radar acquisitions due to the field of view. Currently, visual inspection is the most effective way for detecting new cracks followed by monitoring of their evolution over the course of time [15]. Typically, a geotechnical engineer walks on the active failing grounds to identify new cracks, and to install surface/subsurface instrumentation directly on the crack for monitoring the evolution, where remote-monitoring may not be feasible based on the sensor type. Manual sensor installation and instrumentation has a number of disadvantage that include requiring extensive amount of human resource and additional sensors, exposing the human resources to unnecessary hazards and risk, rendering measurements to sparse locations in the open-pit mine, and hindering quantitative analysis on the morphology and scale of cracks.

This article presents a new methodology for automated identification and monitoring of tension cracks in open-pit mines. It involves scanning the open-pit mine at a constant elevation with an unmanned aerial vehicle (UAV). The acquired video stream images are combined and distortions are corrected using photogrammetry. The results are then extracted as an orthomosaic image (OI) and digital elevation map (DEM) of the mine. First, the DEM is used to isolate and delineate distinct regions of the mine corresponding to the ramps and work- and catch-benches. Both work- and catch- benches are excavated at constant elevations, but the ramps provide access to different areas of the mine. The net result is a list of center-lines that are computed from segmentation of the DEM. Second, computed center-lines are represented as way-points, uploaded to the UAV, and the UAV is programmed to scan work- and catch-benches at high resolution. These high-resolution images are then processed for crack detection.

A. Related Work

In this section, a brief review is provided for the application of UAVs in open-pit mines followed by a summary of current methods on crack detection.

The utility of UAVs in the mining applications has been increasing rapidly in recent years. By coupling video streams with flight planning and postprocessing, a large mosaic image and the corresponding elevation map can be constructed. For example, (i) in [23], drone photogrammetry was used for optimum placement of blasting holes during open-pit mining operations; (ii) in [24], UAVs were used for geomorphic hazard for increased safety; and (iii) in [25], UAVs were used to recreate a model of the open-pit mines.

More recently, computer vision methods have been applied for crack detection in different media, which include buildings, roads, and manufacturing processes. The methodologies are based on image binarization, iterative voting, and deep learning. The readouts include a stationary camera within controlled environment, mobile laser scanning (MLS), or aerial photography with a UAV. In [26], a UAV was used to scan the exterior of a concrete building to detect cracks using a hybrid image binarization via multiple thresholds. This methodology works well for images with relatively uniform background, (e.g., no shading, uniform illumination), and low texture environment. In [27], concrete road corridors were scanned using MLS technology and surface cracks were detected using the iterative voting method [28]. In [29], impurities in the manufacturing of metal components were detected using a fusion of deep learning and a naive Bayes classifier. Image binarization is not appropriate for open-pit mines because the background may be textured, corrupted with shading, or contain natural (e.g., shadows created by large rocks) or man-made artifacts (e.g., tire marks of heavy machinery). Iterative voting is applied to a cloud of points that are collected by a laser scanner, but cracks computed from the elevation map have a very low contrast. These are the gaps that we will address with the proposed methodologies.

The novelty of our approach is an *integrated system* for identifying tension cracks in open-pit mines. This system 1) couples flight trajectory of a drone with photogrammetry for construction of a 3-D topography of the mine at low resolution, 2) computes a semantic representation (e.g., work benches, ramps) from the 3-D topography of the mine, 3) generates a second flight trajectory so that benches can be mapped at high resolution, and 4) identifies and delineates tension cracks from high resolution images.

This article is organized as follows. Section II provides the details of the proposed solution. Section III concludes this article.

II. Materials and Methods

A. Evaluation Metrics

The evaluation metrics for segmentation of cracks was based on pixel- and object-level using F1-score and aggregated Jaccard index (AJI) [30], respectively. The F1-score was calculated from precision and recall per Equations (1)–(3). Precision is a measure of positive predictive value and is defined by the ratio of correctly classified crack pixels to all classified crack pixels. Recall is a measure of sensitivity and is defined by the ratio of correctly classified crack pixels to the number of true crack pixels. AJI builds on the computed Jaccard Index (JI), shown in (4), for one-object at a time. First, corresponding annotated and predicted objects are registered. Second, the JI computes an index, between 0 and 1, based on the correct and incorrect segmentation. Third, computation of JI is aggregated for all objects.

$$\text{Precision} = \frac{\text{True Positive}}{\text{True Positive} + \text{False Positive}} \tag{1}$$

$$\text{Recall} = \frac{\text{True Positive}}{\text{True Positive} + \text{False Negative}} \tag{2}$$

$$F1 = 2 * \frac{\text{Precision} * \text{Recall}}{\text{Precision} + \text{Recall}} \tag{3}$$

$$J(A, B) = \frac{|A \cap B|}{|A \cup B|}. \tag{4}$$

TABLE I
SUMMARY OF DJI MAVIPRO EQUIPMENT SPECIFICATIONS

Max Flight Time	27min	**Image Size**	4000x3000 pixels
Navigation	GPS + GLONASS	**Weight**	734g
Battery	3830 mAh 11.4V	**Charging Time**	45min
Max Altitude	120m	**Max Speed**	40 mph

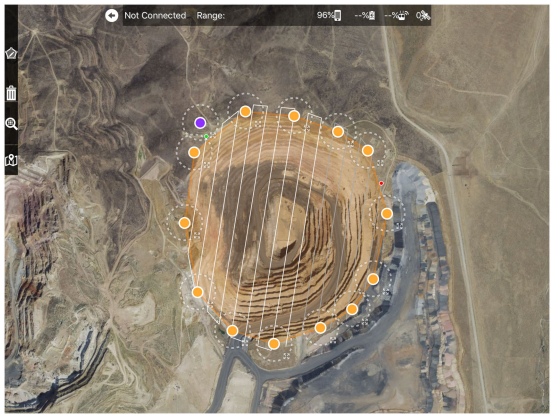

Fig. 1. An example of the user interface for the maps made easy iOS app, where the purple and orange circles define the home base and the boundaries of the open-pit mine, respectively. The white lines are the operator-defined UAV path and the app automatically computes the way-points.

TABLE II
FLIGHT PLANNING DETAILS FOR 3-D MODELING MISSION

Flight Planning			**Imaging**		
	Pit A	Pit B		Pit A	Pit B
Altitude (AGL)	120 m	120 m	**Forward Overlap**	80%	80%
Area	50.2 hect	249.7 hect	**Side Overlap**	70%	70%
Max Speed	9.6 m/s	9.6 m/s	**Number of Images**	437	2012
Flight Time	28min	132min	**Dimensions**	682x518 m	659x1093 m

B. Representation of the Open-Pit Mines

Two open-pit mines, with diverse geometries and soil textures, were scanned by a UAV. The detailed protocol for construction of the image mosaic and DEM is reported along with the spatial statics of each open-pit mine.

The DEM of each open-pit mine was constructed using a UAV flown at a constant elevation over the entire pit. The protocol was tested on two open-pit mines of the size 50 and 250 hectors using a DJI Mavic Pro UAV at undisclosed locations. The specification for this commercially available UAV is summarized in Table I. The flight trajectory was interactively designed and executed using the maps made easy iOS application. First, an operator used the app to overlay of the flight trajectories over Googlemaps, as shown in Fig. 1. Second, the operator specified parameters associated with the flight planning and image collection as specified in Table II. The app then directed the UAV to collect consecutive images, along the specified trajectory, and stored images on a local disk. Additionally, several ground control points (GCPs) were marked and surveyed throughout the mine, where were used for validating the reconstruction.

The following protocol was developed for reconstruction of an open-pit mine from a UAV video stream, which is visualized in Fig. 2. Having collected the image sequences and GCPs, the next

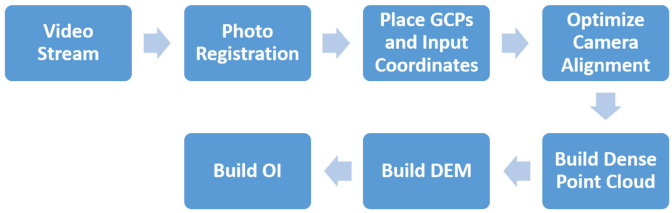

Fig. 2. Protocol for reconstruction of an open-pit mine from a UAV video stream resulting in OI and DEM images.

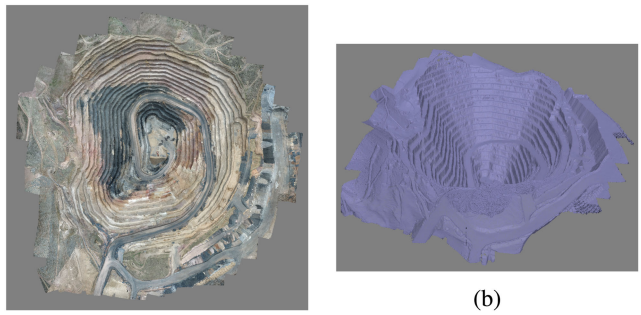

(a) (b)

Fig. 3. Agisoft PhotoScan constructs a (a) rendered OI, and (b) DEM.

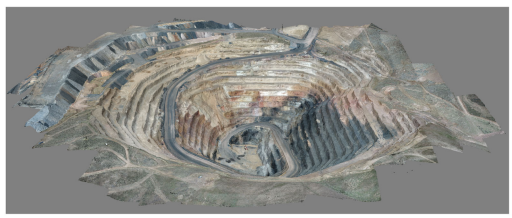

Fig. 4. Rendering the OI with the DEM yields an interactive 3-D model of the pit.

TABLE III
SUMMARY OF 3-D MODEL CONSTRUCTIONS FOR TWO OPEN-PIT MINES

Model	**Resolution**		**Processing Time**	
	Pit A	Pit B	Pit A	Pit B
Point Cloud	67.5 pt/m^2	40.7 pt/m^2	3h 42min	31h
Digital Elevation Map (DEM)	12.2 cm/pixel	15.7 cm/pixel	2min 8sec	1min
Orthomosaic Image (OI)	12.2 cm/pix	15.7 cm/pix	10min 39sec	14min 56sec

step was to construct an OI and the corresponding DEM. The OI and DEM were constructed using the commercially available Agisoft PhotoScan module [31]. This module takes in the series of geo-tagged images, gathered during the modeling flight, and generated a single OI and its corresponding DEM, as shown in Figs. 3 and 4. All processing was performed with a single 8GB Nvidia GeForce GTX 1080 GPU with the details of processing times shown in Table III.

Reconstruction of the OI and DEM were validated by the Agisoft PhotoScan software via 1) the GPS information for each image, and 2) 12 control points that were manually surveyed in the open-pit mine. Agisoft software first computed the location

TABLE IV
ELEVATION STATISTICS FOR PITS A AND B AFTER RECONSTRUCTION

	Pit A	Pit B
Elevation mean (m)	1615	1471
Elevation std	47.6	80.7
KS-test p-value	0.0	

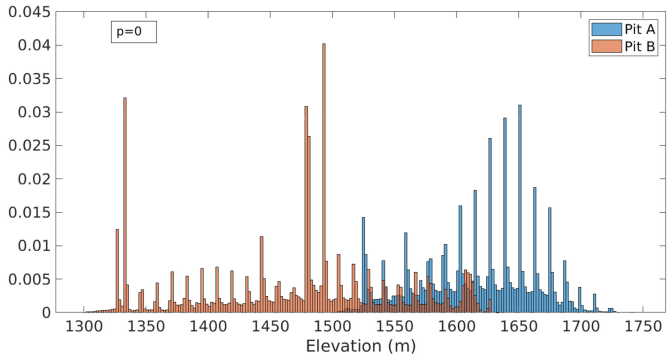

Fig. 5. Elevation PDFs for each reconstructed pit DEM shows that the two are statistically different with a ks-test *p*-value of 0.0.

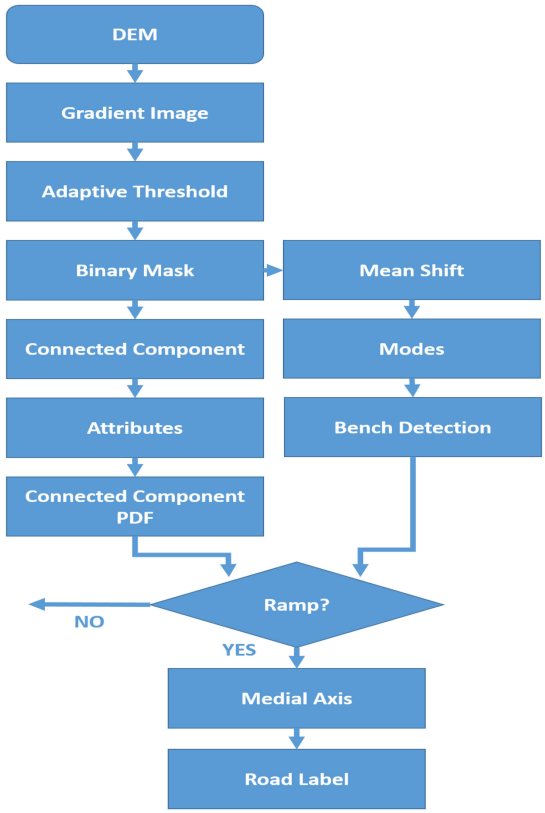

Fig. 6. Flowchart indicating the protocol for bench detection, bench identification, and ramp identification.

of each pixel in terms of latitude, longitude, and elevation for the OI and DEM, and then computed the error between estimated image location and the actual GPS measurement from the drone. The GPS, on the drone, has an accuracy of +/−5 meters. For pit A, the mean and standard deviations of error for longitude, latitude, and elevation were 1.6±0.34, 0.542 ±0.72, and 23.97±0.20 meters, respectively. The reason for a high error rate in the elevation map is due to the onboard inaccurate barometer measurements.

Using the DEM reconstructed image, open-pit mines were statistically assessed for their dissimilarity. Statistical measures included first- and second-order statistics as shown in Table IV. Furthermore, similarity between two open-pit mines was assessed using the nonparametric, two-sided, KS-test based on computed probability density functions (pdf) of each open-pit mine as shown in Fig. 5.

C. Labeling Benches and Ramps

In the section, we summarize the protocol for labeling of benches and ramps from the DEM.

Labeling of different geometrical structures of the open-pit mines such as benches and ramps are essential because tension cracks are developed in those regions. This is well accepted in the field and has to do with the inherent instability that may be caused as a result of excavation. It has also been established that tension cracks may have different signatures for ramps and benches [2], [14]. Furthermore, because of the heavy mine traffic, on ramps, no safety risk can be tolerated [14]; hence, the detection of tension cracks becomes even more necessary.

The protocol, shown in Fig. 6, delineates benches and represents ramps with medial axis using a cascade of low and mid-level image operators on the DEM. The large-scale DEM images were partitioned into an initial binarized mask that was further refined using higher level analysis. Connected components of this initial mask are referred to as super segments, which were subsequently labeled as either a bench or a ramp.

Computation of super-segments takes advantage of the engineering design for construction of the open-pit mine and intrinsic properties of the DEM. These super-segments do not necessarily provide an accurate representation; however, any ambiguities were resolved with higher level constraints. The sources of inaccurate representation were often due to erosion and fallen rocks. During construction, catch- or working-benches are excavated on horizontal planes, at approximately equal height intervals, and separated by faces. Ramps are constrained to provide access roads to various locations in the open-pit mine. When mapped by DEM, access roads were constrained to be geometrically smooth and be invariant to shadows; hence, facilitating ramp detection. Bench and ramp delineation took 62 and 101 s for Pits A and B, respectively.

While there are a number of possible methodologies for segmentation, we opted for an approach where the large-scale DEM were first partitioned into manageable super-segments followed by applications of low- and high-level reasoning. The simplest approach for generating the super-segments was to convolve the DEM with a Gaussian first-derivative operator at an appropriate scale. Typically, mines are excavated with benches being 10–15 m wide and faces being approximately 11 m long. With a window size of 73-by-73 pixels, the coverage area will be approximately 5-by-5 m, which was about half the width

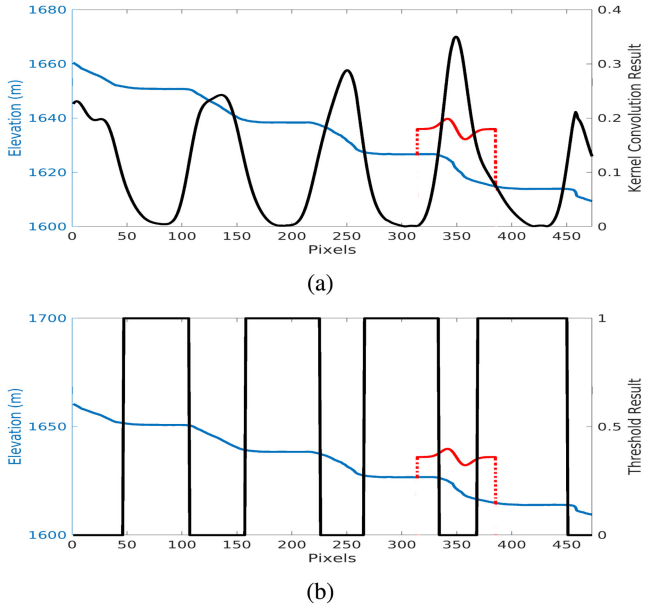

Fig. 7. A profile view of DEM benches (blue) with an overlaid first derivative Gaussian kernel (red) showing the maximum possible kernel size in relation to the physical width of a bench. (a) Shows a 1-D profile in blue, the kernel in red, and the convolution results in black. (b) Shows thresholded convolution results.

of a face or a bench. Fig. 7 shows the results of convolving a filter with the profile of a bench in Pit A. This window size provided favorable local support for noise suppression and accurate localization of edges, i.e., location of the edge being shifted as a result of the cross-talk between adjacent edges at the crest and toes. Finally, the window size of 73-by-73 pixels translates to a Gaussian $\sigma = 8$.

Hence, by taking advantage of the spatial smoothness of benches and ramps, separated by sharp faces in DEM, regions of high gradient were isolated. The gradient image was subsequently binarized using the adaptive thresholding algorithm [32]. This algorithm was used to assign a pixel as a foreground or background pixel by comparing it to a computed average of its local neighborhood. Additionally, by adding a scalar to the computed average, the sensitivity of a pixel to its local neighborhood can be controlled. Results of this protocol, for six randomly chosen patches from Pits A and B, are shown in Fig. 8.

The protocol requires two free parameters of "neighborhood size" (aka window size) and "sensitivity" (as defined in MATLAB) in the adaptive thresholding algorithm, which were empirically (e.g., search and parameter tuning) determined. These parameters were chosen by first selecting a region of the open-pit mine that was highly effected by changes in these parameters, i.e., a high "sensitivity" and low window size resulted in fragmented benches. Next, the AJI was computed for a range of sensitivity values and window sizes, where the results are shown in Table V. Finally, the parameters 513 and 0.3 produced the best AJI-score and were selected for processing of both Pits.

1) Segmentation of Benches: Super-segments can be erroneous as a result of rockfalls or intersection of benches with the

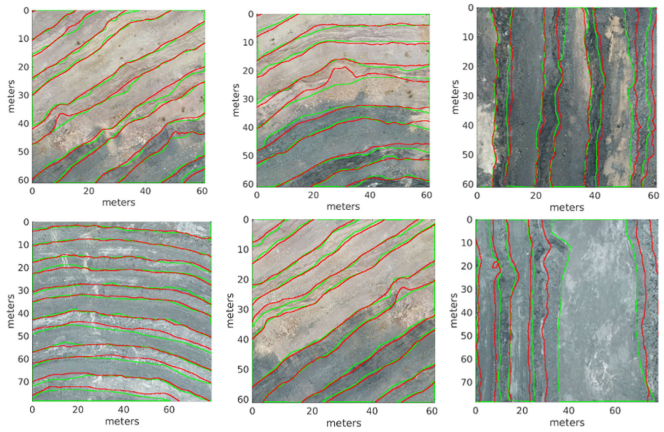

Fig. 8. Comparison of manually annotated (green) and automatically detected (red) bench boundaries shows the difficulty in manually delineating benches from faces in RGB images.

TABLE V
FREE PARAMETERS OF THE ADAPTIVE THRESHOLD ALGORITHM WERE EMPIRICALLY DETERMINED BY MAXIMIZING THE AJI-SCORE

		Window Size						
		17	33	65	129	257	**513**	1025
Sensitivity	0.2	0.096	0.096	0.131	0.286	0.729	0.738	0.725
	0.3	0.096	0.098	0.175	0.728	0.734	**0.738**	0.726
	0.4	0.095	0.122	0.270	0.726	0.735	0.734	0.722
	0.5	0.116	0.131	0.461	0.717	0.727	0.725	0.711
	0.6	0.496	0.579	0.649	0.696	0.708	0.701	0.687
	0.7	0.148	0.417	0.573	0.597	0.675	0.612	0.644
	0.8	0.053	0.257	0.512	0.562	0.584	0.556	0.535

access road that cause adjacent benches, at different elevations, to be merged. This ambiguity can be resolved by perceiving each bench, at a specific elevation, with a unique "mode" and utilizing the mean shift algorithm [33]. The mean-shift algorithm identified distinct modes in the elevation data, and assigned each mode a unique label. As a result, two benches that were merged erroneously via an access ramp were partitioned based on their elevation differences and unique labels were assigned to each bench. To speed up the processing time, spatial data were sampled without the loss of performance on the segmentation result. Examples, for two different open-pit mines, are shown in Figs. 11(b) and 12(b), where each bench is uniquely labeled according to the corresponding mode in the mean-shift algorithm.

2) Segmentation of Ramps: Within a single open-pit, there were two types of super-segments: 1) corresponding to constant-height catch-benches; and 2) ramps that provide road access to different regions of the mine. The boundaries between these two were often blurred, ambiguous and lead to incorrect segmentation results, i.e., portions of the ramp may be assigned to a catch bench or vice-versa. However, delineating ramps cannot be resolved without integration of high-level attributes.

For each super-segment, a pdf was computed from the corresponding elevation points, which we refer to as elevation map pdf (em-pdf). Fig. 9 shows a significant difference between the em-pdf of benches and ramps, where a simple second-order statistic, such as standard deviation, was sufficient to discriminate ramps and benches. Since, all active open-pit mines must contain at

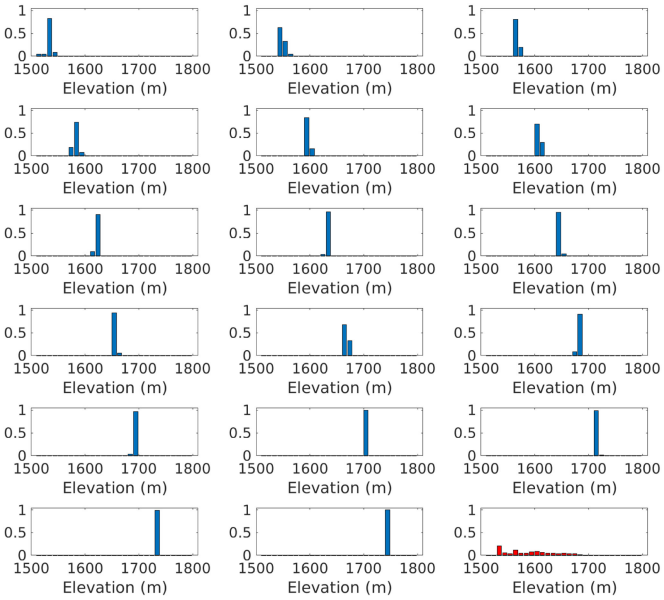

Fig. 9. PDFs of benches and ramps can easily be differentiated. The first 17 PDFs, shown in blue, correspond to benches and the last one, in red, corresponds to a ramp.

least one ramp for access and material removals, two different clusters of em-pdf must be present in every open-pit mine. These clusters were identified by the application of k-means on the standard deviation of em-pdf. To eliminate the effects of random initialization, the two clusters were initialized with the minimum and maximum values of standard deviation in the sample pool.

Once super-segments containing a ramp have been identified, the corresponding medial axes (e.g., the centerlines) were extracted such that the path corresponds to the ramp. The medial axis, for each super-segment, was computed using a skeletonization method [34] and endpoints were then computed and organized by their associated elevation. A pair of endpoints was chosen by their largest difference in elevation, and the shortest path along the skeleton was computed [35].

Fig. 6 shows the protocol for bench and ramp identification. Fig. 10 visualizes the intermediate results for ramp detection: super-segment image with identified segments based on em-pdf; skeletonized segments; and the final ramp path. Figs. 11 and 12 show the final bench and ramp detections for Pits A and B, respectively.

D. Topographic Flight Path Generation

To collect high-resolution images of benches for crack detection, the UAV was reprogrammed to follow and scan the work- or catch-benches at a specific altitude for a specific resolution. A natural choice for following a path along a bench, at a constant altitude, was the bench centerline. However, this computation is not trivial as benches may not be continuous (e.g., eroded benches and fallen rock) and segmentation results may not yield smooth boundaries. Hence, to compute reliable centerlines, super-segments were skeletonized [34], the endpoints computed and localized, a cost function was computed for each pair of

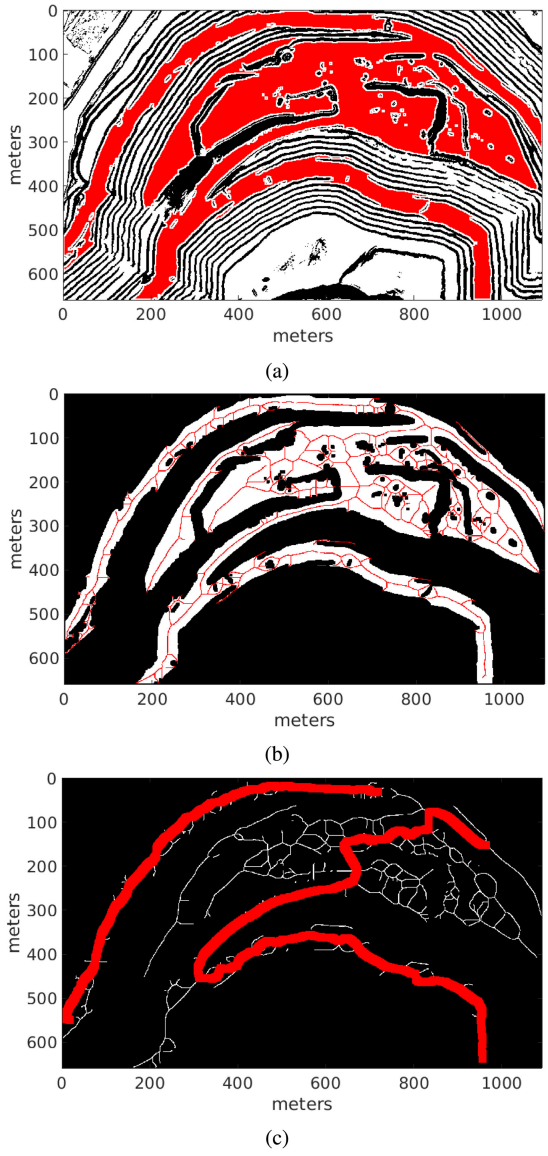

Fig. 10. Intermediate steps of the ramp-detection protocol shows detection of ramps from a bench super-segments. (a) Overlays super-segment regions (red) on the super-segment map. (b) Overlays the medial axes (red) of each super-segment on the map. (c) Overlays computed ramp path (red) on the map.

endpoints based on the minimum path, and the optimum path was selected.

Suppose that for an arbitrary pair of endpoints, $[x_i \quad x_j]$, there is a finite set of paths, P, along the skeleton that link the two endpoints together, $P = \{p_1, p_2, \ldots, p_k\} \mid k \in [1, K]; K < \infty$. Then the cost function for the pair of endpoints is

$$C_{ij} = \min_{p \in P} ||p_k|| \tag{5}$$

where $||p_k||$ is the absolute length of path p_k.

Finally, each centerline was converted into a series of GPS coordinates that can be uploaded to the UAV. This protocol is shown in Fig. 13. Additionally, one of the side effects of computing the flight path from the elevation map is an added

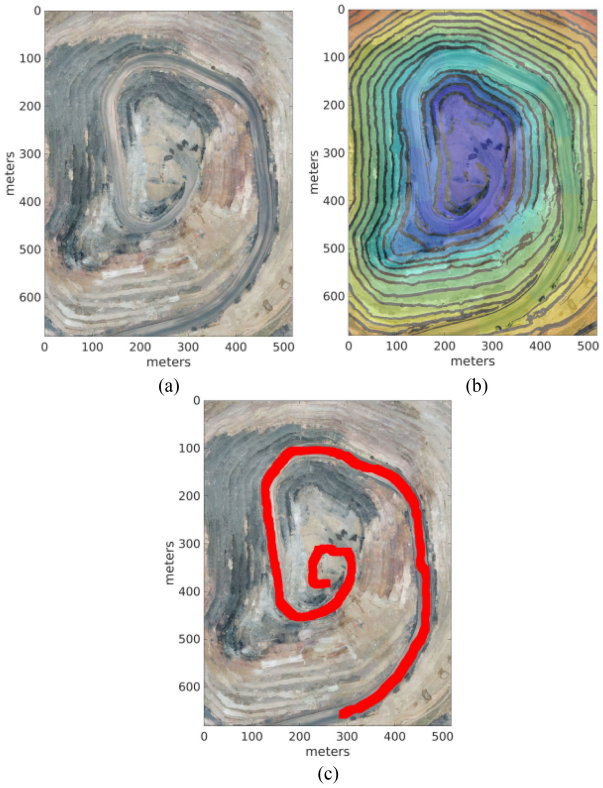

Fig. 11. A cropped region of "Pit A" shows: (a) OI. (b) OI with bench delineations. (c) OI with ramp detection. For the purpose of visualization, segmentation has been rendered with the original color of the OI.

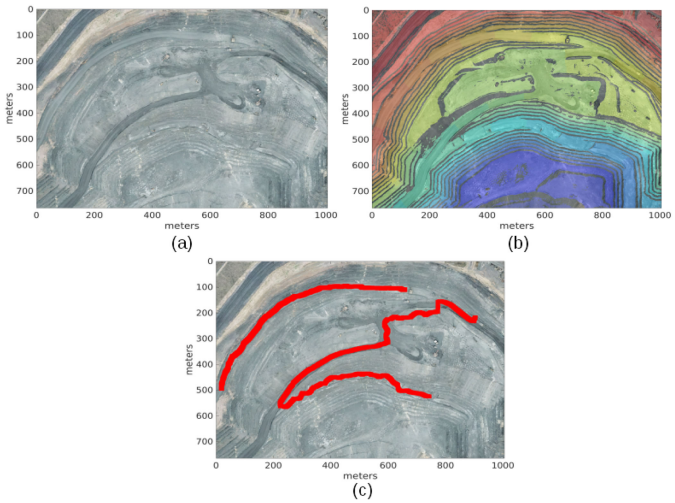

Fig. 12. A cropped region of "Pit B" shows: (a) OI. (b) OI with bench delineations. (c) OI with ramp detection. For the purpose of visualization, segmentation has been rendered with the original color of the OI.

redundancy to the on-board collision avoidance sensors and software.

E. Crack Detection and Characterization

Crack detection has been evaluated using procedural and deep-learning models. Procedural methods use steerable filters,

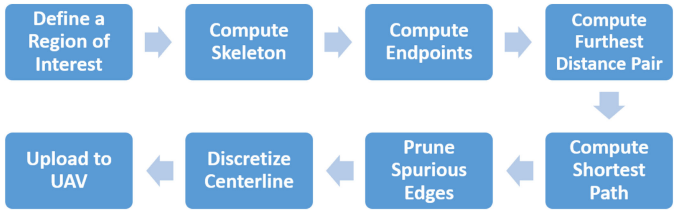

Fig. 13. Flowchart indicating the protocol for generating a region of interest way-points from the super-segments of a bench.

which must be coupled with perceptual grouping. The rationale for perceptual grouping is that the cracks are not necessarily continuous and postprocessing is needed. The deep-learning approach uses a variant of instant-based segmentation for high throughput processing given the massive amount of data. In both cases, high-resolution OI requires large amounts of computational RAM for image analysis. To alleviate this constraint, an OI was tiled into smaller patches that easily fit into RAM and processed. This sliding window approach is commonly used in many applications for analyzing large images.

1) Steerable Filters: Cracks in work- and catch-benches can be detected by their pixel intensities and elongated shape. Their unique geometrical structures justifies application of steerable filters [36] (e.g., a bank of filters) that modulate filter shape with different elongations, orientations, and scales. Each filter was a 2-D kernel defined by the second-derivative of two 1-D Gaussian filters in the x- and y-directions. The main advantage is that these filters are separable; hence, high throughput processing was assured. The Sigma of Gaussian defines the scale (e.g., the width of the gap), and was modulated from 5 to 20 (e.g., 19.6–78.3 cm). Filter orientation was modulated every 10° in the intervals between 0° and 360°. This protocol produced 118 filters, each filter was applied to the image, and an output where each pixel corresponds to maximum response was aggregated into a single image for thresholding. A companion image also saved the orientation for maximum response at each pixel location.

The filter bank was effective in terms of capturing cracks; however, it suffers from false positives, cracks can be fragmented, and higher level processing would be required. The higher level processing would be in terms of perceptual grouping of the medial axis in a delineated graph [28] or shortest path algorithm. However, these results are not reported here because steerable filters suffer from a significant amount of false alarm, as discussed later.

2) Convolutional Neural Networks: Deep learning models are used in many different computer vision applications, and perform particularly well in image segmentation. Within the deep learning framework, convolutional neural networks with a encoder–decoder architecture are specialized for image segmentation. The ENet [37] and UNet [38] architectures are well known models in the literature. Each architecture was implemented in accordance with their respective manuscripts; however, the size of the input and output images were reduced from 512-by-512 to 380-by-380. ENet (efficient neural network) was originally developed for mobile applications by reducing

TABLE VI
HYPERPARAMETERS USED TO THE TRAIN ENET ARCHITECTURE

Hyper-parameters	
learning rate	5e-4
learning rate weight decay	2e-4
weight decay	2e-4
epochs before decay	100
total epochs	150
batch size	10

TABLE VII
EVALUATION OF SEGMENTATION PERFORMANCE FOR VARIOUS METHODOLOGIES SHOWS ENET AS THE FAVORABLE APPROACH

Model	AJI	F1-score
Steerable Filter Bank	0.27 ± 0.15	0.52 ± 0.20
UNet	0.30 ± 0.01	0.61 ± 0.08
ENet	$\mathbf{0.41 \pm 0.05}$	$\mathbf{0.69 \pm 0.03}$

TABLE VIII
LEAVE-ONE-OUT PERFORMANCE FOR THE ENET ARCHITECTURE

AJI	F1-score
0.51 ± 0.20	0.79 ± 0.06

the number of required complex operations, and is also referred to as "instant-based segmentation." Its architecture consists of encoder (e.g., compression) and decoder (e.g., segmentation) layers. Each layer consists mainly of 5×5, 5×1, 1×5, 3×3, 3×1, 1×3, or 1×1 convolutions with a total of 17 layers. Due to small window-size convolutions, the processing time for each patch was approximately 78 ms. Training of the ENet was performed with a mini-batch size of 10, an adaptive moment estimation (ADAM) optimizer, and the hyperparameters listed in Table VI.

For training and testing, 74 images were annotated. These images include patches with and without cracks. All data were collected by a UAV at six independent locations with altitudes ranging from 16 to 135 m above the surface. OIs were generated, by the same protocol for open-pit mine, and arranged in patches of 380-by-380 pixels. Annotated images were divided into training and testing sets with the ratio 85–15%, respectively. Data augmentation was then utilized to extend the number of training images by 14-fold and included: rotations, flipping, contrast alteration, noise additions, and warping. Performance was assessed using AJI and F1-Score. Table VII summarizes the performance of each predictive model in terms of AJI and F1-Score following extensive cross validation and Fig. 14 highlights key examples of each model's predictive abilities. Having validated the ENet superior performance, leave-one-out cross-validation method on the original 74 images was also performed. The Leave-one-out is an unbiased estimator of the generalization error [39], and produced an improved performance of 0.51 AJI score, as shown in Table VIII.

III. RESULTS AND DISCUSSION

This article has provided an approach to integrate aerial surveillance of open-pit mines with visual analytics for routine monitoring of tension cracks for mine safety. First, a 3-D reconstruction of the open-pit mine was created using video

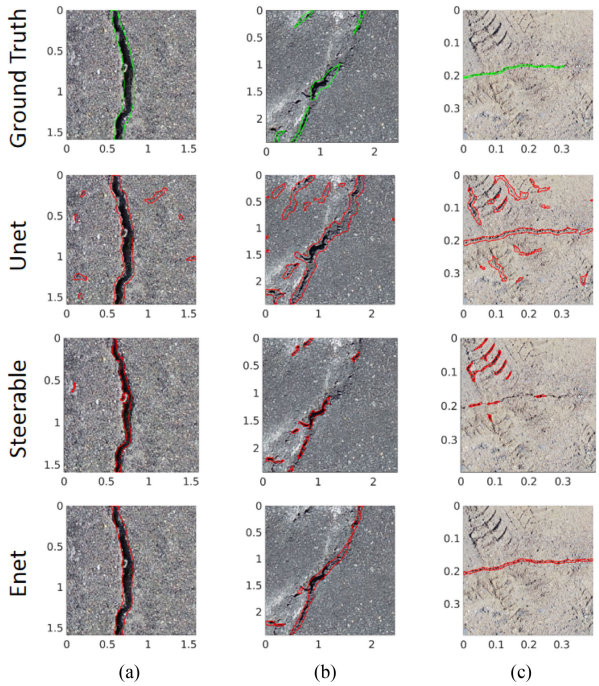

Fig. 14. ENet had the best performance for crack detection for a diversity of spatial signatures. (a) High contrast crack against low textured background. (b) Fragmented crack with possible erosion. (c) Thin crack next to tire marks resembling cracks.

surveillance from a UAV; from which intrinsic properties of spatial organization of the DEM were computed. These properties were then utilized to take high-resolution video surveillance of areas prone to tension-cracks and eventual failures (e.g. working- and catch-benches). Bench detection was validated against manual annotations with a reported AJI score of 0.84. Second, three visual analytic models, based on procedural and learning techniques, were used to automatically delineate tension cracks from high-resolution video streams. ENet produced the best segmentation performance of the tension crack images with 85–15% of the data decomposed for training and testing followed by cross validation. Subsequently, the leave-one-out method increased the performance further in terms of AJI and F1-score, which suggests that model construction can benefit from a larger sample size.

Comparison of the computed AJI and F1-score, for each of the three crack delineation methods, showed that ENet outperforms other methods for segmenting tension cracks, as shown in Table VII. Examples of the model predictions are shown in Fig. 14, where patches were selected to highlight the differences between each model's predictive abilities: Fig. 14(a) shows a simple example of a single crack; Fig. 14(b) shows an example of a fragmented crack; and Fig. 14(c) shows a thin crack in the context of neighboring tire marks. These examples indicate that steerable filters suffer high false alarm rate and that the segmentation accuracy will be further compromised following perceptual grouping. However, the encoder–decoder architecture of ENet was better capable to learn scale of the cracks, perform grouping of cracks, and remain insensitive to artifacts such as tire marks.

Future work involves (i) collecting additional data for improved tension crack segmentation, and (ii) monitoring the crack evolution over time. In (i), tension crack images will be collected under different conditions (e.g., cloudy days, varying sun positions, wet, and dry soil) to add to the diversity of testing data. A subset of data with poor performance will then be annotated and the ENet model will be retrained for improved robustness of the model. In (ii), crack monitoring was not performed due to the lack of data representing the dynamics of crack evolution. If the evolution of tension cracks can be monitored then these indices can also be integrated with the risk or hazard prediction.

References

[1] A. Vaziri, L. Moore, and H. Ali, "Monitoring systems for warning impending failures in slopes and open pit mines," *Natural Hazards*, vol. 55, no. 2, pp. 501–512, 2010.

[2] J. Read and P. Stacey, "Guidelines for open pit slope design," CSIRO Publishing, 2009. [Online]. Available: https://doi.org/10.1071/9780643101104

[3] G. J. Dick, E. Eberhardt, A. G. Cabrejo-Liévano, D. Stead, and N. D. Rose, "Development of an early-warning time-of-failure analysis methodology for open-pit mine slopes utilizing ground-based slope stability radar monitoring data," *Can. Geotechni. J.*, vol. 52, no. 4, pp. 515–529, 2014.

[4] T. Carlà, P. Farina, E. Intrieri, H. Ketizmen, and N. Casagli, "Integration of ground-based radar and satellite InSAR data for the analysis of an unexpected slope failure in an open-pit mine," *Eng. Geol.*, vol. 235, pp. 39–52, 2018.

[5] D. K. Yadav, G. Karthik, S. Jayanthu, and S. K. Das, "Design of real-time slope monitoring system using time-domain reflectometry with wireless sensor network," *IEEE Sens. Lett.*, vol. 3, no. 2, pp. 1–4, Feb. 2019.

[6] R. Lynch, R. Wuite, B. Smith, and A. Cichowicz, "Microseismic monitoring of open pit slopes," in *Proc. 6th Symp. Rockbursts Seismicity Mines*, 2005, pp. 581–592.

[7] J. Armstrong and N. Rose, "Mine operation and management of progressive slope deformation on the south wall of the Barrick goldstrike betze-post open pit," in *Proc. Int. Symp. Rock Slope Stability Open Pit Mining Civil Eng., Santiago*, 2009.

[8] C. Atzeni, M. Barla, M. Pieraccini, and F. Antolini, "Early warning monitoring of natural and engineered slopes with ground-based synthetic-aperture radar," *Rock Mech Rock Eng.*, vol. 48, no. 1, pp. 235–246, 2015.

[9] J. Doyle and J. Reese, "Slope monitoring and back analysis of east fault failure, Bingham canyon mine, utah," in *Proc. Slope Stability 2011: Int. Symp. Rock Slope Stability Open Pit Mining Civil Eng.*, Vancouver, Canada, 18–21 Sept., 2011, Paper 269.

[10] P. Farina*et al.*"Recent advances in slope monitoring radar for open-pit mines," *Proc. Mine Closure Solutions*, 2014.

[11] P. Farina, N. Coli, R. Yön, G. Eken, and H. Ketizmen, "Efficient real time stability monitoring of mine walls: The çöllolar mine case study," *Int. Mining Congr. Exhib*, 2013, pp. 111–117.

[12] A. Ginting, M. Stawski, and R. Widiadi, "Geotechnical risk management and mitigation at grasberg open pit, pt freeport Indonesia," in *Proc. Slope Stability 2011: Int. Symp. Rock Slope Stability Open Pit Mining Civil Eng.*, Vancouver, Canada, 18–21 Sept. 2011, Paper 122.

[13] J. M. Girard, "*Assessing and monitoring open pit mine highwalls*," in *Proc. 32nd Annu. Inst. Mining Health, Saf. Res.*, Salt Lake City, Utah, 5–7 Aug. 2001, pp. 159–171.

[14] W. A. Hustrulid, M. K. McCarter, and D. J. Van Zyl, *Slope Stability in Surface Mining*. Dearborn, MI, USA: SME, 2001.

[15] A. Kumar and V. G. Villuri, "Role of mining radar in mine slope stability monitoring at open cast mines," *Proc. Earth Planetary Sci.*, vol. 11, pp. 76–83, 2015.

[16] G. Macqueen, E. Salas, and B. Hutchison, "Application of radar monitoring at savage river mine, tasmania," in *Proc. Slope Stability*, 2013, pp. 1011–1020.

[17] G. Antonello *et al.*, "Ground-based SAR interferometry for monitoring mass movements," *Landslides*, vol. 1, no. 1, pp. 21–28, 2004.

[18] F. Bardi *et al.*, "Monitoring the rapid-moving reactivation of earth flows by means of GB-InSAR: The april 2013 capriglio landslide (Northern Appennines, Italy)," *Remote Sensing*, vol. 9, no. 2, 2017, Art. no. 165.

[19] N. Casagli *et al.*, "Spaceborne, UAV and ground-based remote sensing techniques for landslide mapping, monitoring and early warning," *Geoenviron. Disasters*, vol. 4, no. 1, 2017, Art. no. 9.

[20] N. Casagli, F. Catani, C. Del Ventisette, and G. Luzi, "Monitoring, prediction, and early warning using ground-based radar interferometry," *Landslides*, vol. 7, no. 3, pp. 291–301, 2010.

[21] G. Luzi *et al.*, "Advances in ground-based microwave interferometry for landslide survey: A case study," *Int. J. Remote Sens.*, vol. 27, no. 12, pp. 2331–2350, 2006.

[22] O. Monserrat, M. Crosetto, and G. Luzi, "A review of ground-based SAR interferometry for deformation measurement," *ISPRS J. Photogrammetry Remote Sensing*, vol. 93, pp. 40–48, 2014.

[23] J. Valencia, R. Battulwar, M. Zare Naghadehi, and J. Sattarvand, "Enhancement of explosive energy distribution using UAVs and machine learning," in *Proc. 39th Int. Symp. 'Appl. Comput. Oper. Res. Minearl Industry*,' 2019, pp. 671–677.

[24] J. Chen, K. Li, K.-J. Chang, G. Sofia, and P. Tarolli, "Open-pit mining geomorphic feature characterisation," *Int. J. Appl. Earth Obser. Geoinform.*, vol. 42, pp. 76–86, 2015.

[25] R. Battulwar, J. Valencia, G. Winkelmaier, B. Parvin, and J. Sattarvand, "High-resolution modeling of open-pit slopes using UAV and photogrammetry," in *Proc. 39th Int. Symp. 'Appl. Comput. Oper. Res. Mineral Industry*,' 2019, pp. 661–670.

[26] H. Kim, J. Lee, E. Ahn, S. Cho, M. Shin, and S.-H. Sim, "Concrete crack identification using a UAV incorporating hybrid image processing," *Sensors*, vol. 17, no. 9, 2017, Art. no. 2052.

[27] H. Guan *et al.*, "Iterative tensor voting for pavement crack extraction using mobile laser scanning data," *IEEE Trans. Geosci. Remote Sens.*, vol. 53, no. 3, pp. 1527–1537, Mar. 2015.

[28] L. A. Loss, G. Bebis, and B. Parvin, "Iterative tensor voting for perceptual grouping of ill-defined curvilinear structures," *IEEE Trans. Med. Imag.*, vol. 30, no. 8, pp. 1503–1513, Aug. 2011.

[29] F.-C. Chen and M. R. Jahanshahi, "Nb-CNN: Deep learning-based crack detection using convolutional neural network and Naïve Bayes data fusion," *IEEE Trans. Ind. Electron.*, vol. 65, no. 5, pp. 4392–4400, May. 2018.

[30] N. Kumar, R. Verma, S. Sharma, S. Bhargava, A. Vahadane, and A. Sethi, "A dataset and a technique for generalized nuclear segmentation for computational pathology," *IEEE Trans. Med. Imag.*, vol. 36, no. 7, pp. 1550–1560, Jul. 2017.

[31] "*Agisoft photoscan professional (version 1.2.6) (software)*," 2016. [Online]. Available: http://www.agisoft.com/downloads/installer/

[32] D. Bradley and G. Roth, "Adaptive thresholding using the integral image," *J. Graphics tools*, vol. 12, no. 2, pp. 13–21, 2007.

[33] Y. Cheng, "Mean shift, mode seeking, and clustering," *IEEE Trans. Pattern Anal. Mach. Intell.*, vol. 17, no. 8, pp. 790–799, Aug. 1995.

[34] L. Lam, S.-W. Lee, and C. Y. Suen, "Thinning methodologies-a comprehensive survey," *IEEE Trans. Ind. Electron.*, vol. 14, no. 9, pp. 869–885, Sep. 1992.

[35] S. Eddins. Exploring shortest paths - part 5. [Online]. Available: https://blogs.mathworks.com/steve/2011/12/13/exploring-shortest-paths-part-5/

[36] W. T. Freeman and E. H. Adelson, "Steerable filters for early vision, image analysis, and wavelet decomposition," in *Proc. 3rd Int. Conf. Comput. Vision*, 1990, pp. 406–415.

[37] A. Paszke, A. Chaurasia, S. Kim, and E. Culurciello, "Enet: A deep neural network architecture for real-time semantic segmentation," 2016, *arXiv:1606.02147*.

[38] O. Ronneberger, P. Fischer, and T. Brox, "U-net: Convolutional networks for biomedical image segmentation," in *Proc. Int. Conf. Medical Image Comput. Computer-Assisted Intervention*, 2015, pp. 234–241.

[39] A. Elisseeff, M. Pontil *et al.*, "Leave-one-out error and stability of learning algorithms with applications," *NATO Science Series Sub Series III Comput. Syst. Sci.*, vol. 190, pp. 111–130, 2003.

Garrett Winkelmaier (Member, IEEE) received the M.S. degree in electrical engineering IN 2018 from the University of Nevada (), Reno, NV, USA, where he developed methods for profiling stain-free tumor samples from hyperspectral imaging. He is currently working toward the Ph.D. degree in biomedical engineering program with UNR.

More recently, his research has focused on integrative analysis of molecular, pathology, and clinical data for identifying tumor biomarkers. He has been a Reviewer for IEEE conferences and recipient of the Wise Trust Graduate School and IGT Peter Dickinson awards.

Rushikesh Battulwar received the M.S. degree in mining engineering from the University of Nevada, Reno, NV, USA, in 2018. He is currently woking toward the Ph.D. degree in mineral resource engineering with the University of Nevada, Reno, NV, USA.

He was a Junior Mining Engineer with Hindustan Zinc Limited, India, from 2016 to 2017. His research includes applications of unmanned aerial vehicles and computer vision for high wall stability in open-pit mines.

Mr. Battulwar is a Student Member of the Society of Mining and Exploration (SME).

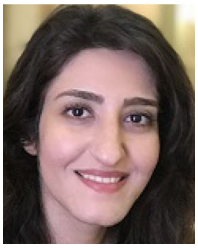

Mina Khoshdeli received the Ph.D. degree in electrical engineering from the University of Nevada, Reno, NV, USA, in 2019.

Her dissertation focused on deep learning models for delineating multiple nuclear phenotypes from different imaging modalities. She is currently a Research Scientist with the Clinical Bioinformatics Department, Gilead Sciences, Inc. Her research interests include the development of predictive models for clinical applications using AI techniques.

Jorge Valencia (Member, IEEE) received the B.Sc. and M.Sc. degrees in mining engineering from the University of Santiago, Chile, USA, in 2006 and 2016, respectively. He is currently working toward the Ph.D. degree in geoengineering with the University of Nevada Reno, Reno, NV, USA.

His area of research includes applications of the integrated drone-based platform and machine learning for blast-hole localization. He is also developing an academic training program at Phoenix Mine–a Nevada Gold Mines Operation.

Mr. Valencia is a member of the Society for Mining, Metallurgy, and Exploration (SME) and the International Society of Explosives Engineers (ISEE).

Javad Sattarvand received the Ph.D. degree in mining engineering from the University of RWTH Aachen, Aachen, Germany in 2009.

From 2000 to 2015, he was a Faculty with Mining Engineering Department, Sahand University, Iran, where he was an Associate Professor. In 2015, he joined the University of Nevada, Reno, Mackay School of Earth Sciences and Engineering, as an Assistant Professor. His research focuses on mining automation and safety.

Prof. Sattarvand is the PI on several Federally funded grants and is a member of the society of Mining and Exploration (SME).

Bahram Parvin (Senior Member, IEEE) received the Ph.D. degree in electrical engineering from the University of Southern California, Los Angeles, CA, USA, in 1991.

In 1992, he joined Lawrence Berkeley National Laboratory as a Principal Scientist. In 2015, he joined the Electrical and Biomedical Engineering Department, University of Nevada, Reno (UNR), and since 2016, he has been the Director of the Biomedical Engineering Department, UNR. He has more than 13k citations and eight patents. Dr. Parvin was the General Chair of IEEE ISBI in 2013, and was the recipient of the R&D100 award in 2014, and is presently a member of the IEEE Biological Imaging and Signal Processing (BISP) Technical Committee.